Time-Frequency Analysis of Seismic Reflection Data

Philippe Steeghs
TNO Physics and Electronics Laboratory
Oude Waalsdorperweg 63
P.O. Box 96864
2509 JG The Hague
The Netherlands
e-mail: steeghs@fel.tno.nl

Richard Baraniuk and *Jan Erik Odegard*
Department of Electrical and Computer Engineering
Rice University
6100 Main Street
Houston TX 77005–1892
e-mail: {richb,odegard}@rice.edu

1 Introduction

In this chapter we will apply quadratic time-frequency representations to the analysis of seismic reflection data. Seismic imaging of the earth's subsurface is an essential technique in exploring for oil and gas accumulations. A seismic image is obtained by probing the subsurface with acoustic waves. An example of a seismic cross section is shown in Fig. 1(b). The horizontal axis is the spatial location at the surface, and the vertical axis is time. Each column in this image represents a recording of the reflected wave amplitude as a function of time at the corresponding surface location.

When seismic waves propagate through the subsurface, energy is reflected back towards the surface at acoustic impedance contrasts. The strength of this impedance contrast is called the *reflectivity*. The seismic cross section of Fig. 1(b) is a representation of the (band-limited) reflectivity of the subsurface. If the seismic wave velocity is known, then the time axis can be converted to depth. In the image of Fig. 1(b), a two-way (down and up) travel time of 1 s corresponds roughly to a depth of 1 km below the surface. When a rapid change in acoustic impedance occurs at a certain depth, this generally implies a change in the composition of the rocks. As a result, it is possible to make an educated guess of the geological structure of the subsurface, based on the seismic image.

In the following we will show how time-frequency analysis of seismic images can help to identify and classify sequences of seismic reflections. The characteristics of such sequences can provide a hint of the geological processes that resulted in the observed reflectivity.

Figure 1(a) is a time-frequency representation of the first vertical time trace of the seismic section of Fig. 1(b). Changes in the time-frequency patterns coincide with boundaries of seismic sequences. The location and distinctive character of the sequences is more pronounced in the time-frequency representation than in the time signal, illustrating the added value of time-frequency analysis for seismic sequence interpretation.

The analysis and classification of seismic waveforms is called *seismic attribute analysis*. Seismic attributes are features extracted from a seismic image that elucidate signal characteristics that are relevant for the geological interpretation of the reflectivity image. Until recent years, the emphasis has been on one-dimensional (1-D) analysis along the vertical (time) axis. This is because the vertical axis corresponds to the chronology of geological events — rocks that were formed longer ago in geological time are found below younger sediments. Nowadays, 3-D seismic data acquisition has become the standard in the petroleum industry. The result is that the volume of data being analyzed has grown tremendously. Paper plots of seismic cross sections have been replaced by gigabytes of image data that are interpreted on computer screens or, increasingly, in immersive visualization environments. Seismic attributes are increasingly important for detection and visualization of subsurface structures that are hidden in these enormous volumes of data. In conjunction with this development, there also has been a shift towards full 3-D feature extraction and analysis. In the last part of this chapter we will discuss 3-D seismic data analysis with extensions of our time-frequency analysis methods to higher dimensions.

2 Seismic sequence analysis

The frequency content of a seismic reflection record is primarily dependent on the bandwidth of the outgoing seismic source pulse and the absorption characteristics of the subsurface. Variations within this band are primarily the result of changes in the timing of seismic reflections. A reflection sequence can be described with attributes such as the continuity, amplitude, and frequency of the reflections. The time-frequency representation of a seismic section brings forward characteristics of the seismic sequence that are not easily observed in the time domain or frequency domain alone. We are mainly interested in localizing strong transitions in frequency characteristics over time, since these transitions indicate where changes occur in the geological circumstances under which the rocks were formed. The more gradual time variations of frequency content in-between these transitions are also of interest, since these may provide clues for relating the signal characteristics to the geological process that resulted in a certain subsurface structure.

Our model of a seismic sequence is that of a layered earth, where each of the layers is bounded by seismic impedance discontinuities. Typically, a sequence will consist of a stack of layers that in turn is bounded at the top and base by a major discontinuity. We will start with an analysis of the time-frequency representation of such a "generic sequence."

Figure 1(a) illustrates a time-frequency representation of the leftmost column of the seismic section to its right (Fig. 1(b)). We observe that the seismic signal is clearly a multicomponent signal. At about $t = 0.3$ s there is a strong impulse-like component; this is a reflection from the strong contrast between water and sea-bottom. The seismic response below the sea-bottom reflection is a complicated interference pattern, resulting from reflections at rock interfaces that cannot be resolved individually. We can subdivide the seismic signal into seismic sequences on the basis of its distinctive time-frequency patterns, which is clearly much easier than subdividing based on the time signal itself.

Figure 2 illustrates the composition of a "generic" seismic time-frequency sequence. We have constructed an impedance model of the subsurface that consists of three types of components. The first component is a rectangular box-car function (Fig. 2(a)) of unit impedance. This homeogenous impedance is perturbed with a purely harmonic impedance variation (a cosine, Fig. 2(b)). We have introduced a frequency change at $t = 0.5$ s. The third component is a perturbation with a linearly increasing frequency (a linear chirp, Fig. 2(c)). The overall, superposition impedance model is shown in Fig. 2(d). The simplest model for the seismic response $u(t)$ to this impedance variation is the reflectivity of the impedance function $r(t)$ convolved with a seismic source signal $s(t)$:

$$u(t) = \int_{-\infty}^{+\infty} r(t')\, s(t-t')\, dt'. \tag{1}$$

The seismic response of the sequence model of Fig. 2(d) is shown in Fig. 2(e).

Figure 3 shows an idealized time-frequency representation of the reflectivity function $u(t)$ of Fig. 2(e). Next to the time and frequency axes of the time-frequency representation, we plot the time signal and the Fourier power spectrum. This idealized time-frequency representation was created by adding the Wigner distributions of the signal components. The components of the impedance model can be easily discerned in the time-frequency image. The top and the base of the sequence give rise to an impulse-line time-frequency pattern, like the sea-bottom reflector in Fig. 1. The harmonic and chirping perturbations of the impedance can also be easily located in the time-frequency plane.

This simple example demonstrates the value of time-frequency analysis over time-domain analysis for seismic sequences. However, the time-frequency representation of the measured seismic data in Fig. 1 shows that seismic reflection signals are clearly multicomponent signals. Moreover, in the example above we synthesized an ideal time-frequency representation by adding the time-frequency representations of the components. For measured data we cannot separate the components beforehand, which makes choosing the proper time-frequency representation an important issue.

3 Time-frequency representations for seismic signal analysis

If we weight the data $u(t)$ at each time t with a window function $w(t)$, we obtain the modified signal

$$u_t(\tau) = u(\tau)\, w(t-\tau). \tag{2}$$

The sliding window Fourier transform is then given by

$$\widehat{u}_t(f) = \int_{-\infty}^{+\infty} u_t(\tau)\, e^{-j2\pi f \tau}\, d\tau. \tag{3}$$

Repeating this procedure for each time t and taking the squared modulus of $\widehat{u}_t(f)$, we obtain the *spectrogram* time-frequency representation

$$S(t,f) = \left|\widehat{u}_t(f)\right|^2. \tag{4}$$

The localization of the spectrogram is strongly influenced by the choice of window function $w(t)$. The windowed signal $u_t(\tau)$ and the local spectrum are a Fourier transform pair. Consequently, their breadth in time and frequency are linked by the uncertainty principle. Figure 4 illustrates this property of the spectrogram. We analyze the synthetic seismic signal of Figure 2(e) with both a short time window (Fig. 4(a)) and a long window (Fig. 4(b)).[1] In the short-window spectrogram we observe that the signal components are well localized in time but poorly localized in frequency. If we increase the window size, frequency localization is improved, but time localization deteriorates. This makes the spectrogram less suited for seismic data analysis, since we require accurate localization of both the sequence boundaries (time localization) and the changing patterns within each sequence (frequency localization).

An effective way to minimize window effects is to match the analysis window to the signal. For certain types of signals, excellent results can be achieved by using the reversed signal as an analysis window, which yields the *Wigner distribution*

$$W(t,f) = \int_{-\infty}^{+\infty} u(t+\tau/2)\, u^*(t-\tau/2)\, e^{-j2\pi f\tau}\, d\tau, \tag{5}$$

where the asterisk denotes complex conjugation.

Figure 4(c) displays the Wigner distribution of the synthetic seismic trace. The energy localization in the time-frequency plane has improved considerably. We can clearly observe a much sharper time-frequency localization compared to the spectrogram. However, oscillating ridges now appear between signal components at (t,f) locations where no energy is expected. These so-called *cross-terms* result from the quadratic nature of the Wigner distribution. Cross-term interference complicates the interpretation of the Wigner distribution of measured seismic signals.

Cross-terms can be largely suppressed by smoothing the Wigner distribution over time and frequency to obtain a new representation

$$P(t,f) = \int_{-\infty}^{+\infty} \int_{-\infty}^{+\infty} \Psi(t',f')\, W(t-t', f-f')\, dt'\, df'. \tag{6}$$

The smoothing function $\Psi(t,f)$ is called the *kernel* of the representation. Each particular kernel results in a different time-frequency representation, whose properties can be derived directly from the kernel. Figure 4(d) shows the *smoothed pseudo-Wigner distribution*, which uses a separable kernel $\Psi(t,f) = h(t)\, G(f)$. In this example we have used Gaussian-shaped time and frequency windows

[1] Note that all of the time-frequency representations that we show in this chapter have been computed using the complex-valued *analytic signal* corresponding to the real-valued signal obtained in the seismic measurement. There are several motivations for using the analytical signal. For instance, its complex valued-ness allows the decomposition in amplitude and phase. Also, the absence of negative frequencies in its Fourier spectrum has certain advantages with respect to both computational efficiency and interpretation of the time-frequency analysis results [1].

for $h(t)$ and $G(f)$. We see that the cross terms are largely suppressed without overly compromising the time and frequency resolution.

The class of time-frequency representations obtained by smoothing the Wigner distribution is called *Cohen's class* [1]. The spectrogram of (4) is also a member of this class, with a kernel that is the Wigner distribution of the analysis window $w(t)$. Taking the 2-D Fourier transform of (6), the convolution of becomes a weighting operation on the characteristic function of time-frequency representation

$$M(\nu, \tau) = \Psi(\nu, \tau)\, A(\nu, \tau). \tag{7}$$

Here $M(\nu, \tau)$ is the characteristic function (Fourier transform of $P(t, f)$), $\Psi(\nu, \tau)$ is the Fourier transform of the kernel, and $A(\nu, \tau)$ is the *ambiguity function* (Fourier transform of the Wigner distribution).

In search of a smoothing kernel adapted to the properties of seismic signals, we aim to maximize the suppression of the cross terms while compromising other desirable properties of the time-frequency representation as little as possible. For instance, there is a trade-off between the degree of cross-term suppression (maximal smoothing) and preserving resolution (minimal smoothing).

The *cone-kernel*

$$\Psi(\nu, \tau) = w(\tau)\ |\tau|\ \frac{\sin(2\pi a \nu \tau)}{2\pi a \nu \tau} \tag{8}$$

appears well suited to seismic data analysis [2]. Here $w(\tau)$ is a real and symmetric window function, and a is a dimensionless constant — typically $a = 1/2$ is taken. The cone-kernel time-frequency representation is depicted in Fig. 4(f). Since the kernel is zero along the frequency-shift (ν) axis, impulse-like signals are suppressed, and components that are parallel to the time axis (harmonics) are emphasized. Thus, this kernel does not smooth impulses, as does the spectrogram, but suppresses them outright. This results in a very effective representation for accurately localizing frequency transitions. However, the chirping component in the signal cannot be very well distinguished in the time-frequency image, since it is not parallel to the time axis.

The location and amplitude of the cross-terms depend on the characteristics of the signal. Consequently, this trade-off can only be optimized by adapting the shape of the smoothing kernel to the characteristics of the signal under analysis. The *adaptive optimum kernel* (AOK) time-frequency representation [3] of the seismic trace is shown in Fig. 4(e). The AOK representation adapts the shape of the kernel at each time instant t to maximally concentrate energy in the time-frequency plane while suppressing cross-terms. In the AOK representation of Fig. 4(e), the cross terms have been largely suppressed, with only minimal resolution deterioration compared to the Wigner distribution. Note that both the short duration signal components (pulses) and long duration components (tones) are localized equally well. It is this ability to sharply localize energy in both time and frequency that makes the AOK very well suited for local spectral analysis of seismic signals.

Figure 5 shows the time-frequency representations of the seismic field data of Fig. 1. Figures 5(a) and 5(b) show the result of spectrogram analyses with a short and long window. It would be very hard to make a meaningful subdivision of the seismic signal on the basis of the spectrograms. The short-window spectrogram shows only the individual reflections, whereas the long-window spectrogram resolves only the individual frequencies and fails to localize the sequence transitions. The Wigner distribution of Fig. 5(c) is difficult to interpret, because it is overwhelmed by cross-terms. Smoothing the Wigner distribution results in an improvement, but it is still difficult to distinguish individual components. The cone-kernel and AOK representations appear to perform the best in terms in separating and localizing seismic sequence patterns in the data (Figs. 5(e) and 5(f)). The cone-kernel time-frequency representation appears well suited for separating the seismic signal into distinct sequences because of the accurate localization of frequency transitions. The AOK representation gives a more balanced picture of the time-frequency properties of the seismic signal. Strong impulse-like signals, such as the sea-bottom reflection, are more clearly imaged, and also components with an increasing or decreasing frequency as a function of time can be observed.

Up to now we have focused on the time-frequency representation of a single seismic trace (a column from the seismic section of Fig. 1(b), for example). However, seismic field data consist of large numbers of traces. It would be impossible for a seismic interpreter to inspect the time-frequency representation of each individual trace from a seismic survey. For this reason, it is desirable to “summarize” a time-frequency representation with a limited number of features. Localization of features in time (and space) is crucial, since there is a one-to-one mapping between the time coordinate and the depth below the earth’s surface. Feature extraction from the time-frequency representation is the subject of the next sections.

4 Seismic attribute extraction

Seismic attributes aid the interpretation of seismic images by elucidating salient signal characteristics. Traditionally, complex-trace analysis via the Hilbert transform has been used for attribute extraction [4]. The standard complex-trace attributes are the instantaneous amplitude (reflection strength), phase, and frequency. Complex-trace attributes are still widely used in seismic signal analysis.

In complex-trace notation, the seismic trace is an analytic signal given by

$$u^a(t) = a(t)\, e^{j2\pi\phi(t)}, \tag{9}$$

where $a(t)$ is the instantaneous amplitude and $\phi(t)$ is the instantaneous phase. The complex-trace *instantaneous frequency* $g(t)$ is the derivative of the instantaneous phase

$$g(t) = \frac{1}{2\pi}\frac{d\phi(t)}{dt}. \tag{10}$$

The instantaneous frequency can be estimated directly using a discretized version of (10). Unfortunately, this estimate is highly susceptible to noise. A more robust estimate of the instantaneous frequency can be formed by considering the relationship between the Wigner distribution and the instantaneous frequency [1], [5]

$$g(t) = \frac{\int_{-\infty}^{+\infty} f\, W(t,f)\, df}{E(t)}, \tag{11}$$

where $E(t) = \int_{-\infty}^{+\infty} W(t,f)\, df$ is the time marginal. Hence, the mean frequency is the first moment of the time-frequency representation, normalized by the energy. Direct utilization of (11) leads to high-variance estimates for noisy signals. However, bias can be traded against variance by replacing the Wigner distribution with a smoothed time-frequency representation $P(t,f)$ from Cohen's class (6).

Figure 6 illustrates the use of a time-frequency representation for seismic attribute extraction. Figure 6 shows a seismic trace and its cone-kernel time-frequency representation. In time-frequency we plot the mean frequency $g(t)$ (solid line) and the standard deviation around the average (dotted line) as a function of time. The standard deviation corresponds to an instantaneous bandwidth. Seismic attribute images can be generated by plotting these time curves in the same manner as the amplitude data in Fig. 1(b).

Figure 7 plots the mean frequency $g(t)$ of each vertical trace in the seismic data of Fig. 1(b) as extracted from four different time-frequency representations: the spectrogram, pseudo smoothed-Wigner distribution, the AOK representation, and cone-kernel representation. Dark values correspond to high attribute values; a linear scaling has been used.

The image of the spectrogram mean frequency in Fig. 7(a) is somewhat blurred, making it difficult to localize the sequence transitions and relate the attribute features to the amplitude data. The smoothed pseudo-Wigner result of Fig. 7(b) clearly shows the major transitions and gives detailed and very well localized frequency information. In the AOK result, we observe more gradual changes in frequency content, similar to the spectrogram attribute image of Fig. 7(a). However, in the AOK result the temporal transitions are also clearly visible. This combination of eliciting both more gradual and instantaneous features makes the AOK representation the best of these four representations for attribute extraction. However, for large data volumes, the computational effort involved in the AOK could become too burdensome for practical application. The cone-kernel result of Fig. 7(d) shows that this TFR is a computationally more attractive alternative to adaptive time-frequency analysis.

Besides the mean frequency, a great number of other signal attributes can be extracted from a time-frequency representation. A straightforward extension is to calculate the higher-order moments. For instance, we can extract an *instantaneous bandwidth* attribute by calculating the variance around the mean frequency $g(t)$

$$B(t)^2 = \frac{\int_{-\infty}^{+\infty} (f - g(t))^2 \, P(t,f) \, df}{E(t)}. \tag{12}$$

Other statistics measures for characterizing density functions include the *skew* and *kurtosis* [6], [7]. Skew measures the deviation of the density function from a normal (Gaussian) distribution and is computed from the third moment around the mean

$$s(t) = \frac{\int_{-\infty}^{+\infty} (f - g(t))^3 \, P(t,f) \, df}{B(t)^3 E(t)}. \tag{13}$$

A positive skew signifies an asymmetric distribution with a tail extending out towards positive frequencies. A normal distribution has zero skew.

Kurtosis measures the peakedness of the distribution and is related to the fourth-order moment [7]

$$k(t) = \frac{\int_{-\infty}^{+\infty} (f - g(t))^4 \, P(t,f) df}{B(t)^4 \, E(t)} - 3, \tag{14}$$

where the term -3 makes the value zero for a normal distribution. Density functions with a positive kurtosis have a more sharply peaked shape than a Gaussian. Negative kurtosis signifies a distribution that is flatter than a normal distribution.

Figure 8 shows four additional attribute images for the seismic section of Fig. 1(b) extracted from the cone-kernel representation. Figure 8(a) plots the *peak frequency* as a function of time. The peak frequency is very well suited for segmenting the section into a limited number of large-scale seismic sequences. However, the peak frequency image lacks the fine detail that can be observed in the mean frequency images of Fig. 7. The sequences boundaries we would define on the basis of the peak frequency image coincide with changes in instantaneous bandwidth values in Fig. 8(b). Some boundaries (at $t = 0.65$ s and $t = 1.25$ s) that are less pronounced in the mean frequency image are clearly visible in the instantaneous bandwidth image.

The instantaneous skew is less sensitive to the transitions in time-frequency patterns, but brings forward the characteristics of the reflectivity between the sequence boundaries. Several intervals can be characterized by their distinctive skew values. For example, between $t = 1$ s and $t = 1.2$ s we have relatively high skew, whereas around $t = 1.6$ s we observe low skew values. High values of kurtosis coincide with more chaotic and noisy reflection patterns in the amplitude data. The laterally continuous reflections around $t = 0.4$ s result in consistently low kurtosis values. Around $t = 0.8$ s , there is a region with more chaotic reflection patterns. Here, we observe also relatively high kurtosis values. Right above $t = 1.4$ s we see two reflectors with a high kurtosis value. In the AOK time-frequency representation of Fig. 1(a), we also observe that the energy is highly concentrated around a single frequency. This is typical for the seismic response to a “thin bed” — a rock layer that is thin with respect to the seismic wavelength ($< \lambda/4$), with a strong reflectivity at the top and the base of the layer [8]. The individual reflections from the top and base of the layer cannot be resolved, but the frequency of the reflection “tunes” to the frequency that corresponds to the (time) thickness of the layer.

These examples demonstrate the utility of time-frequency representations for seismic interpretation and attribute extraction. However, the computational effort of calculating a representation for each seismic trace may be a serious impediment to using this method on large seismic data volumes. A typical seismic data volume consists of several million traces, each of approximately one thousand samples. Fortunately, for time-frequency representations with a fixed kernel, it is in many cases possible to calculate the attribute moments directly without calculating the highly redundant time-frequency representation itself. In the next section we present an efficient method for robustly calculating the signal attributes using the principles of hybrid linear/quadratic time-frequency analysis.

5 Hybrid linear/quadratic time-frequency seismic attributes

In this section, we present a computationally efficient method for estimating moment-based time-frequency attributes that avoids the calculation of a quadratic time-frequency representation altogether. Our approach exploits the *time-frequency distribution series* concept developed by Qian, Morris, and Chen [9], [10], [11] and requires only a sparse linear signal decomposition. We will present a general procedure for calculating a range of attributes, but focus on instantaneous frequency and bandwidth estimation for concreteness.

Qian, Morris, and Chen proposed a method for time-frequency analysis that uses both a linear time-frequency basis representation (the Gabor transform) and a quadratic time-frequency representation (the Wigner distribution) to generate a signal-adaptive nonlinear time-frequency representation. The Gabor transform decomposes a signal $u(t)$ in terms of logons [12] or time-frequency atoms [12]:

$$\begin{aligned} u(t) &= \sum_{(m,n)} c_{m,n}\phi_{m,n}(t), \quad (m,n) \in \mathbb{Z}^2, && (15)\\ c_{m,n} &= \left\langle u, \widetilde{\phi}_{m,n} \right\rangle = \int_{-\infty}^{\infty} u(t)\, \widetilde{\phi}^*_{m,n}(t)\, dt. && (16) \end{aligned}$$

The synthesis atoms are generated by time-frequency shifting a prototype atom $w(t)$ by discrete step sizes T and F:

$$\phi_{m,n}(t) = e^{j2\pi mFt}\, w(t - nT). \tag{17}$$

The $\widetilde{\phi}(t)$ are dual atoms derived from $\phi(t)$ [9], [12]. A natural choice for the prototype atom $w(t)$ is the Gaussian, since it has optimal concentration and localization in time-frequency and a strictly positive Wigner distribution [1]. For (15) to be a stable representation with Gaussian atoms requires a mild oversampling in the time-frequency plane ($TF < 1$).

The auto-Wigner distribution $W_u(t, f)$ of a signal $u(t)$ is defined in (5); the *cross-Wigner distribution* between two signals $u(t)$ and $v(t)$ is defined as

$$W_{uv}(t, f) = \int_{-\infty}^{\infty} u\,(t + \tau/2)\; v^*\,(t - \tau/2)\; e^{-j2\pi f\tau}\, d\tau. \tag{18}$$

Inserting (16) in (5) and using (18), the auto-Wigner distribution can be decomposed as:

$$\begin{aligned} W_u(t, f) &= \sum_{(m,n)} |c_{m,n}|^2\, W_{\phi_{m,n}}(t, f) \\ &\quad + \sum_{(m,n)\neq(m',n')} c_{m,n}\, c^*_{m',n'}\, W_{\phi_{m,n},\phi_{m',n'}}(t, f). && (19) \end{aligned}$$

This expression identifies two distinct contributions to the Wigner distribution. The first summation in (19) corresponds to a linear sum of the (strictly positive) auto-Wigner distributions of the time-frequency atoms; it provides an approximate description of the signal's time-frequency behavior without capturing many details. The second summation involves all of the cross-Wigner distributions between different atoms in the Gabor decomposition. The cross-Wigner distributions in this summation may take on both positive and negative values.

The key observation is this [9], [10]: the cross-Wigner distributions between closely spaced atoms ((m,n) close to (m',n')) generally refine the time-frequency representation of the signal, whereas the cross-Wigner distributions between distant atoms ((m,n) far from (m',n')) generate global interference terms that hamper interpretation.

Qian, Morris, and Chen generate a time-frequency distribution series — which we term a *hybrid time-frequency representation* [11] — by retaining all of the auto-Wigner distribution terms in the first summation of (19), but only those cross-Wigner distributions arising from closely spaced atoms. Due to the elliptical or circular symmetry of the Gaussian atom, the Euclidean distance metric is the most natural measure of atom separation; the l_1 metric (Manhattan distance) $d\,[(m,n),(m',n')] := |m-m'| + |n-n'|$ is a good approximation with a lower computational complexity. Given a threshold distance δ, second summation terms are included in the final representation only if the distance between the interacting atoms is less than δ. The hybrid method thus produces a δ-parameterized class of time-frequency representations:

$$\begin{aligned} \widetilde{W_u}^{(\delta)}(t,f) \quad &:= \quad \sum_{(m,n)} |c_{m,n}|^2 \, W_{\phi_{m,n}}(t,f) \\ &\quad + \sum_{0<d[(m,n),(m',n')]<\delta} c_{m,n}\, c^*_{m',n'}\, W_{\phi_{m,n},\phi_{m',n'}}(t,f). \end{aligned} \tag{20}$$

The parameter δ controls the trade-off between component resolution and cross-component interference. By a suitable selection of δ, high resolution time-frequency representations are generated; moreover they can be determined at a much lower computational expense than signal-adaptive quadratic time-frequency representations offering similar performance (the AOK, for example). The auto- and cross-Wigner distributions in (20) are signal-independent and hence can be analytically computed and stored in memory. The computational demands of the Gabor transform are also much lower than those of quadratic time-frequency representations. By replacing the Gabor decomposition with a wavelet transform, we can generate high-resolution, low-interference time-scale representations [11].

We now detail how the hybrid time-frequency representation approach can be adopted to robustly estimate the instantaneous frequency and instantaneous bandwidth. Our approach requires the much lower computational expense of determining a linear, mildly over-sampled Gabor representation of the signal.

Substituting (19), we can rewrite the numerator of (11) as

$$\sum_{(m,n,m',n')} c_{m,n}\, c^*_{m',n'} \int_{-\infty}^{\infty} f\, W_{\phi_{m,n}\phi_{m',n'}}(t,f)\, df. \tag{21}$$

When we use a Gaussian of variance σ^2 for the Gabor synthesis atom, closed-form expressions can be developed for the integrals in this summation.[2] Applying the same expansion to the denominator, we can express (11) as

$$g(t) = \frac{\sum_{m,n,m',n'} c_{m,n}\, c^*_{m',n'}\, V_{m,n,m',n'}(t)}{\sum_{m,n,m',n'} c_{m,n}\, c^*_{m',n'}\, A_{m,n,m',n'}(t)} \tag{22}$$

with

$$A_{m,n,m',n'}(t) = \frac{1}{2\pi} \exp[-j2\pi(n-n')Ft]\; \exp\left[-\frac{(t-mT)^2 + (t-m'T)^2}{2\sigma^2}\right] \tag{23}$$

and

$$V_{m,n,m',n'}(t) = \left[\frac{-j(m-m')T}{4\pi\sigma^2} - \frac{(n+n')\,F}{2}\right] A_{m,n,m',n'}(t). \tag{24}$$

If all (m,n,m',n') combinations are included in the estimate, then this formula is equivalent to the (noise-sensitive, high-variance) Wigner distribution-based estimate in (11). By adopting the hybrid time-frequency representation approach (retaining only a subset of the terms when $(m,n) \neq (m',n')$), we can reduce the variance with the introduction of some bias. The performance is of a level similar to that obtained with the AOK time-frequency representation; however, the computational expense is much reduced, since the $A_{m,n,m',n'}(t)$ and $V_{m,n,m',n'}(t)$ are signal-independent and can be pre-computed and stored in memory. The primary cost of the algorithm is then that of computing the (barely oversampled) Gabor transform coefficients $c_{m,n}$.

The second-order moment of the hybrid time-frequency representation provides a similarly computationally efficient estimate for the instantaneous bandwidth:

$$B^2(t) = \frac{\sum_{m,n,m',n'} c_{m,n}\, c^*_{m',n'}\, D_{m,n,m',n'}(t)}{\sum_{m,n,m',n'} c_{m,n}\, c^*_{m',n'}\, A_{m,n,m',n'}(t)} - g^2(t) \tag{25}$$

[2] Similar analytic expressions are possible for other windows, including, for example, the square, triangle, raised cosine, and Jones multiplexed windows.

with

$$D_{m,n,m',n'}(t) = \frac{1}{(4\pi)^2} \exp\left[-\frac{(t-mT)^2 + (t-m'T)^2}{2\sigma^2}\right] \exp[-j2\pi(n-n')Ft] \times \left[-\frac{(T(m-m'))^2}{\sigma^4} + \frac{2+4\pi jTF(m-m')(n+n')}{\sigma^2} + 4\pi^2 \left(F(n+n')\right)^2\right]. \quad (26)$$

We can provide no strict guidelines regarding the choice of the distance threshold δ. If the hybrid estimate is formed without cross-terms (that is with $\delta = 0$, then attribute performance is very similar to the spectrogram. In We have observed that Manhattan distance thresholds δ between 1 and 3 provide good results in our experiments. Setting $\delta = 1$ results in more smoothing and hence more robust estimates in very noisy environments. The choice of $\delta = 3$ reduces the bias of estimates and is appropriate when there is little noise and a single dominant signal component.

It is straightforward to extend this method to other higher-order moments such as instantaneous skew (13) and instantaneous kurtosis (14) in a similar fashion, but the third- and fourth-order terms generate more complicated expressions that we do not provide here.

Figure 9 compares the instantaneous frequency estimates from three different time-frequency representations for the seismic trace of Fig. 1(b). The fast hybrid instantaneous frequency estimate is very close to that obtained using the much more computationally expensive AOK representation. The time resolution of the spectrogram instantaneous frequency estimate is significantly poorer than the other two methods.

Figures 10(a) and (b) show complex-trace instantaneous frequency (10) vs. the hybrid instantaneous frequency estimate (22) for the seismic section of Fig. 1(b). The wild fluctuations indicate that the complex-trace instantaneous frequency estimate is very noise-sensitive. The sharp peaks in the complex-trace instantaneous frequency estimate obscure the frequency trends of interest for a seismic sequence analysis. Comparing Fig. 10 with Fig. 8, we see that the detail and robustness of the hybrid instantaneous frequency estimate is again close to that of the AOK-based estimate. For visual interpretation, the hybrid instantaneous frequency provides a greatly enhanced image as compared to the complex-trace instantaneous frequency or the spectrogram average. This estimation algorithm potentiates the time-frequency-based interpretation of large seismic data volumes, which up to now have been severely inhibited by the large computational effort involved in calculating time-frequency representations.

6 3-D Seismic Attribute Extraction

Three-dimensional seismic data acquisition is currently the standard in the seismic industry. The added value that the 3-D view of geology provides is far greater than the extra cost of data acquisition. However, a consequence of the more detailed subsurface picture is that the volumes of seismic data oil company geologists need to sift through and interpret have grown tremendously. In order to facilitate the interpretation of these large 3-D data volumes, a number of novel techniques for seismic feature extraction and visualization are being developed. Extensions of seismic attribute techniques to higher dimensions is a logical step for improving the extraction and processing of geological information from 3-D seismic data volumes.

The success of seismic volume attribute extraction has demonstrated that the extra information in 3-D data can only be fully exploited if the feature extraction is also fully 3-D — that is, we must move from 1-D time trace attributes to 3-D volume attributes. Volume-dip [13], [14], [15] and coherence [16] [17] attributes illustrate how rapid changes in the characteristics of the 3-D signal generally indicate a geological discontinuity. It is this one-to-one relation of signal characteristics with geological features that underlies the added value of seismic attribute images. In this section we will introduce a seismic volume attribute extraction technique that extends the 1-D attributes we discussed in the previous section.

The starting point of our volume attribute extraction procedure is an analysis of the seismic data with a 3-D *local Radon transformation*. The Radon transformation is used in a wide range of seismic processing and analysis applications. The main reason for its popularity is that it decomposes the data into its plane-wave components [18], [19], [20]. For seismic interpretation purposes, a local Radon transformation would be preferred; often it is not sufficient to know which plane wave components are present in the data, but also where they occur. Local Radon transformations have been defined and applied for different purposes [21], [22], [23]. These local Radon representations are all based on applying the classical "slant stack" to windowed portions of the data. However, in the same way the spectrogram is a member of Cohen's class of time-frequency representations, the sliding-window Radon spectrum is just one choice from an infinite number of local Radon transforms. The Wigner-Radon representation we propose as a candidate for the local slant-stack power spectrum emerges naturally from the definition of the local wavenumber-frequency power spectrum.

Let $u(\boldsymbol{x}, t)$ denote the 3-D seismic signal, with $\boldsymbol{x} = \{x, y\}$ the spatial coordinate vector and t the time coordinate. The Radon transform of $u(\boldsymbol{x}, t)$ is defined as

$$\breve{u}(\boldsymbol{p}, \tau) = \int_{-\infty}^{+\infty} u(\boldsymbol{x}, \tau + \boldsymbol{p} \cdot \boldsymbol{x})\, d\boldsymbol{x}. \tag{27}$$

The vector $\boldsymbol{p} = \{p_x, p_y\}$ represents the slopes of the signal with respect to the (x, y)-plane in the x and y directions, and τ is the intercept with the time axis. In this formulation the Radon transformation essentially sums the signal along lines with slopes $\boldsymbol{p}$ and intercept τ. This interpretation explains the term "slant stack" that is widely used in exploration seismology for this quantity.

The Radon transform of a signal is closely related to its Fourier transform. The Fourier transform of (27) with respect to intercept time τ is given by

$$\breve{u}(\boldsymbol{p}, f) = \int_{-\infty}^{+\infty} \widehat{u}(\boldsymbol{x}, f)\, e^{j2\pi f \boldsymbol{p} \cdot \boldsymbol{x}}\, d\boldsymbol{x}, \quad f > 0, \tag{28}$$

where $\widehat{u}(\boldsymbol{x}, f)$ denotes the temporal Fourier transform of $u(\boldsymbol{x}, t)$. In all practical cases $u(t)$ is either real-valued or a complex-valued analytic signal. In both cases we can restrict the analysis to positive temporal frequency f. Equation (28) is a 3-D Fourier transform of $u(\boldsymbol{x}, t)$. It follows that we can obtain the temporal frequency domain representation of the Radon transform from the 3-D Fourier transform $\tilde{u}(\boldsymbol{k}, f)$ of the signal $u(\boldsymbol{x}, t)$

$$\breve{u}(\boldsymbol{p}, f) = \tilde{u}(f\boldsymbol{p}, f) = \tilde{u}(\boldsymbol{k}, f), \quad f > 0, \tag{29}$$

where $\boldsymbol{k} = \{k_x, k_y\} = f\boldsymbol{p}$ is the spatial frequency vector. This relation leads us to the definition of a local Radon power spectrum that is based on the multi-dimensional Wigner distribution of the signal u.

The 3-D instantaneous autocorrelation function is defined as

$$R(\boldsymbol{x}, t; \boldsymbol{\xi}, \tau) = u(\boldsymbol{x} + \boldsymbol{\xi}/2, t + \tau/2)\, u^*(\boldsymbol{x} - \boldsymbol{\xi}/2, t - \tau/2), \tag{30}$$

where $\boldsymbol{\xi} = \{\xi_x, \xi_y\}$ and τ are the space and time shift variables, respectively. The 3-D Fourier transform over the space shifts $\boldsymbol{\xi}$ and time shift τ yields the Wigner distribution

$$W(\boldsymbol{x}, t; \boldsymbol{k}, f) = \iint_{-\infty}^{+\infty} R(\boldsymbol{x}, t; \boldsymbol{\xi}, \tau)\, e^{j2\pi(\boldsymbol{k}\boldsymbol{\xi} - f\tau)}\, d\boldsymbol{\xi}\, d\tau. \tag{31}$$

We can now obtain a local Radon power spectrum $Q(\boldsymbol{x}, t; \boldsymbol{p}, \tau)$ by invoking relation (29) followed by an inverse Fourier transform

$$Q(\boldsymbol{x}, t; \boldsymbol{p}, \tau) = \int_0^{\infty} W(\boldsymbol{x}, t; \boldsymbol{p}, f)\, e^{j2\pi f\tau}\, df. \tag{32}$$

For seismic attribute extraction we do not perform this inverse Fourier transformation but instead take the average of the local Radon power spectrum with frequency

$$Q(\boldsymbol{x}, t; \boldsymbol{p}, \tau = 0) = \int_0^\infty W(\boldsymbol{x}, t; \boldsymbol{p}, f)\, df. \tag{33}$$

The two basic seismic attributes that we extract from this spectrum are the local average slopes p_x and p_y of the signal. The average slope p_x in the x direction is given by

$$p_x(\boldsymbol{x}, t) = \frac{\iint p_x Q(\boldsymbol{x}, t; \boldsymbol{p})\, d\boldsymbol{p}}{\iint Q(\boldsymbol{x}, t; \boldsymbol{p})\, d\boldsymbol{p}}. \tag{34}$$

In seismic interpretation, the parameters *dip* and *azimuth* are commonly used to describe local geometrical features. The volume dip is the modulus of the local slopes, given by

$$|p| = (p_x^2 + p_y^2)^{1/2}. \tag{35}$$

The azimuth angle is the direction of the signal in the (horizontal) (x, y)-plane. The local average azimuth α is given by

$$\alpha = \tan^{-1}\left(\frac{p_x}{p_y}\right). \tag{36}$$

With the relation of the local Radon power spectrum to the Wigner distribution, we have all the tools and techniques that have been developed for Cohen's class time-frequency representations at our disposal. In a practical implementation, we first compute a multidimensional time-frequency representation and then obtain the local Radon representation by interpolating the wavenumber-frequency spectrum onto a grid of $(\boldsymbol{p}, f)$ coordinates. This has the advantage that efficient FFT-based computational algorithms for time-frequency analysis can be used. A disadvantage is that the interpolation step introduces errors; using more sophisticated interpolation methods greatly increases the computational load. Alternatively, the local Radon spectrum can be computed by directly performing a slant-stack of the local auto-correlation function. For the 3-D sliding-window slant-stack, a fast recursive algorithm has been developed, which is based on a recursive implementation of the the DFT [24], [13].

Figures 11 and 12 illustrate the volume attribute extraction procedure. The data volume is a cube of with dimensions $(n_x, n_y, n_t) = (64, 64, 64)$. The signal is 3-D complex exponential with a constant temporal frequency f_0. In the horizontal direction, the spatial frequency is constant in the radial direction $r = (x^2 + y^2)^{1/2}$. Figures 11(a)—(c) show three slices through this volume. In a seismic data volume, Fig. 11(a) would represent a time-slice, while Figs. 11(b) and 11(c) would be vertical cross-sections or seismic lines. Figures 11(c)-(e) show three slices through the 3-D pseudo-Wigner distribution of the data cube at the locations that are denoted A, B, and C in the data slices. The slices are taken at frequency f_0 and show the localization the spatial frequencies in the horizontal, (x, y), plane. The next step in the attribute extraction procedure is the computation of the local Radon representation $Q(\boldsymbol{x}, t; \boldsymbol{p})$. Figure 11(f) shows the p_x marginal of this local Radon spectrum along a line of constant y and t, cutting through point B in the data cube. The (x, p_x)-spectrum is obtained by summing the Radon spectrum over p_y. Note that the slope p_y of the signal does not change along this line through the data volume. The image shows how the energy is concentrated at a single constant slope and changes sign at the center of the data cube (B). Figure 11(g) shows the (y, p_y)-spectrum of the signal along a line of constant x and t that cuts through point A. The slope of the signal varies gradually with spatial location y.

Figure 12 shows the attributes extracted from the local Radon spectrum. The average local slopes in the x and y directions are shown in Figs. 12(a) and (b). The modulus of the slope (volume dip) and azimuth angle are shown in Figs. 12(c) and (d). The volume dip is constant, except at the center of the time slice (B), where the sign change occurs. The azimuth indicates the direction of the signal with respect to "North" and is constant along radial lines originating from the center of the slice.

Results from a real seismic data volume are given in Figs. 13 and 14. Figure 13(a) shows a time slice through a seismic data cube from the North Sea. The spatial sample spacing is 25 m in x and y and the time sampling is 4 ms. The average slope attributes were extracted from a 3-D smoothed pseudo-Wigner distribution. The size of the autocorrelation cube was $(m_x, m_y, m_t) = (7, 7, 7)$, corresponding to 150 m in the horizontal directions and 24 ms in the vertical direction. The smoothing kernel was 3 samples in all directions. Figure 13(b) shows the slope of the signal in the y direction. White values denote negative slopes, indicating that the signal locally slopes upwards in time and consequently towards lower depths. In this way the slope attribute image gives an impression of the 3-D geometrical properties of the seismic reflections, and thus the geological structure. Figure 14(a) shows the average volume dip, which gives an indication of the steepness of the seismic reflections. Signal discontinuities, such as faults or chaotic reflections, are indicated by high volume dip values (shown in black). The azimuth attribute is shown in Fig. 14(b) and highlights changes in the direction of the slope, giving a view of the general structure but also indicating small-scale faulting.

In Fig. 15 we compare the results obtained with four different local Radon representations. The volume dip map of a part of the time slice of Fig. 13(a) is shown. Figure 15(a) shows the result that is obtained using the 3-D spectrogram. The pseudo-Wigner distribution and smoothed pseudo-Wigner distribution results are shown Figs. 15(b) and (d), respectively. Figure 15(c) shows the attribute image obtained using a 3-D version of the modified Wigner distribution of Stankovič et al. [25]. The smoothed pseudo-Wigner distribution and spectrogram results are very similar. However, in the smoothed pseudo-Wigner result transitions in reflector slope can be more accurately localized. The pseudo-Wigner distribution is more susceptible to noise, which masks several geologically interesting features in the attribute image. The 3-D modified Wigner distribution results in an attribute image that mixes the properties of the pseudo-Wigner distribution and spectrogram images.

7 Conclusions

In this chapter, we have overviewed a number of applications of time-frequency representations in seismic data processing, from the analysis of seismic sequences to efficient attribute extraction to 3-D attributes for volumetric data. Time-frequency representations provide a new physically relevant domain from which to extract information on the earth's subsurface. As the accuracy of time-frequency attributes increases and their computational cost decreases, they are poised to play a central role in the seismic interpretation process. Finally, we note that it is also possible to define instantaneous attributes in terms of time-scale representations such as the wavelet transform; promising results in this direction have recently been developed [26],[27],[28].

References

[1] L. Cohen, *Time-Frequency Analysis.* Prentice Hall, 1995.

[2] Y. Zhao, L. Atlas, and R. Marks, "The use of cone-shaped kernels for generalized time frequency representations of nonstationary signals," *IEEE Trans. Signal Proc.*, vol. 38, pp. 1084–1091, 1990.

[3] D. Jones and R. Baraniuk, "An adaptive optimal kernel time-frequency representation," *IEEE Trans. Signal Processing*, vol. 43, no. 10, pp. 2361–2371, 1995.

[4] T. Taner, F. Koehler, and R. Sheriff, "Complex seismic trace analysis," *Geophysics*, vol. 44, pp. 1041–1063, 1979.

[5] P. Flandrin, *Time-frequency/Time-scale Analysis.* San Diego: Academic Press, 1999.

[6] D. Childers, *Probability and Random Processes.* Irwin, 1997.

[7] P. Loughlin and K. Davidson, "Instantaneous kurtosis," *IEEE Signal Proc. Letters*, vol. 7, pp. 156–159, June 2000.

[8] J. Robertson and H. Nogami, "Complex seismic trace analysis of thin beds," *Geophysics*, vol. 49, no. 4, pp. 344–352, 1984.

[9] S. Qian and J. Morris, "Wigner distribution decomposition and cross-terms deleted representation," *Signal Processing*, vol. 27, pp. 125–144, May 1992.

[10] S. Qian and D. Chen, "Decomposition of the Wigner distribution and time-frequency distribution series," *IEEE Trans. Signal Processing*, vol. 42, pp. 2836–2842, Oct. 1994.

[11] M. Pasquier, P. Gonçalvès, and R. Baraniuk, "Hybrid linear/bilinear time-scale analysis," *IEEE Trans. Signal Processing*, vol. 47, pp. 254–259, Jan. 1999.

[12] D. Gabor, "Theory of communication," *J. IEE*, vol. 93, pp. 429–444, 1946.

[13] P. Steeghs, J. Fokkema, and G. Diephuis, "Local Radon power spectra for 3-D seismic attribute extraction," in *SEG 68th Ann. Internat. Mtg.*, pp. 645–648, Soc. Expl. Geophys., 1998.

[14] P. Steeghs, "A fast algorithm for dip and azimuth computations," in *SEG 69th Ann. Internat. Mtg.*, pp. 1146–1149, Soc. Expl. Geophys., 1999.

[15] P. Steeghs, I. Overeem, and S. Tigrek, "Seismic volume attribute analysis of the Cenozoic succession in the L08 block (Southern North Sea)," *Global and Planetary Change*, vol. 27, pp. 245–262, 2000.

[16] K. Marfurt, R. Kirlin, S. Farmer, , and M. Bahorich, "3-D seismic attributes using a semblance-based coherency algorithm," *Geophysics*, vol. 63, pp. 1150–1176, 1998.

[17] A. Gersztenkorn and K. Marfurt, "Eigenstructure-based coherence computations as an aid in 3-D structural and stratigraphic mapping," *Geophysics*, vol. 64, pp. 1468–1479, 1999.

[18] P. Stoffa, P. Buhl, J. Diebold, and F. Wenzel, "Direct mapping of seismic datato the domain of intercept time and ray parameter – a plane wave decomposition," *Geophysics*, vol. 46, pp. 255–267, 1981.

[19] R. Phinney, K.R.Chowdhury, and L. Frazer, "Transformation and analysis of record sections," *J. of Geoph. Res.*, vol. 86, pp. 359–377, 1981.

[20] S. Treitel, P. Gutowski, and D. Wagner, "Plane wave decomposition of seismograms," *Geophysics*, vol. 47, pp. 175–1401, 1982.

[21] G. McMechan and R. Ottolini, "A direct observation of a p–τ curve in a slant stacked wavefield," *Bulletin of the Seismological Society of America*, vol. 70, pp. 775–789, 1983.

[22] B. Milkereit, "Decomposition and inversion of seismic data — an instantaneous slowness approach," *Geophysical Prospecting*, vol. 35, pp. 875–894, 1987.

[23] A. Copeland, G. Ravichandran, and M. Trivedi, "Localized Radon transform-based detection of ship wakes in SAR images," *IEEE Trans. on Geoscience and Remote Sensing*, vol. 33, pp. 33–45, 1995.

[24] A. Papoulis, *Signal Analysis.* McGraw-Hill Inc., 1977.

[25] S. Stankovič, L. Stankovič, and Z. Uskovič, "On the local frequency, group shift, and cross-terms in some multi-dimensional time-frequency distributions: A method for multi-dimensional time-frequency analysis," *IEEE Trans. Signal Proc.*, vol. 43, pp. 1719–1724, 1995.

[26] R. L. C. van Spaendonck and R. Baraniuk, "Directional scale analysis for seismic interpretation," in *SEG 69th Ann. Internat. Mtg.*, pp. 1844–1847, Soc. Expl. Geophys., 1999.

[27] R. L. C. van Spaendonck, F. C. A. Fernandes, M. Coates, and C. S. Burrus, "Non-redundant, directionally selective, complex wavelets," in *IEEE Proc. Int. Conf. Image Processing Extended Abstracts II*, pp. 379–382, IEEE, 2000.

[28] F. C. A. Fernandes, R. L. C. van Spaendonck, M. Coates, and C. S. Burrus, "Directional complex-wavelet processing," in *Proceedings of SPIE 2000*, vol. 4119, pp. 61–61, 2000.

Figure Captions

Figure 1 : Figure 1: (a) Time-Frequency representation of a the leftmost seismic trace (column) of the seismic cross-section image shown in (b).

Figure 2 : Synthetic model of a seismic sequence with building blocks: (a) layer of unit impedance, (b) harmonic impedance fluctuation (a cosine), and (c) component with increasing impedance as a function of depth (a chirp). (d) The sum of the three components. (e) The seismic reflection response. frequency

Figure 3 : Idealized time-frequency representation of the seismic response to the sequence of Fig. 2. The time signal is shown to the left of the TFR and the power spectrum above. The time-frequency representation has been obtained by summing the Wigner distributions of the seismic responses to the sequence components of Fig. 2(a)—(c).

Figure 4 : Time-frequency representations of the seismic response to the sequence model of Fig. 2: (a) spectrogram with a short window, (b) spectrogram with a long window, (c) Wigner distribution, (d) smoothed pseudo-Wigner distribution, (d) AOK representation, (e) cone-kernel representation.

Figure 5 : Time-frequency representations of the leftmost seismic trace of the seismic cross-section of Fig. 1(b). (a) Spectrogram with a short window, (b) spectrogram with a long window, (c) pseudo-Wigner distribution, (d) smoothed pseudo-Wigner distribution, (d) AOK representation TFR, (e) cone-kernel representation.

Figure 6 : (left) Seismic trace and (right) cone-kernel time-frequency representation with (solid line) instantaneous frequency and (dashed lines) instantaneous bandwidth attributes.

Figure 7 : Seismic attribute images of the seismic cross section of Fig. 1(b). The mean frequency attribute extracted using the (a) spectrogram, (b) smoothed pseudo-Wigner distribution, (c) AOK representation, and (d)cone-kernel representation. Black values represent high frequencies.

Figure 8 : Seismic attribute images of the seismic cross-section of Fig. 1b. computed using the cone-kernel representation. (a) Peak frequency, (b) instantaneous bandwidth, (c) instantaneous skew, and (d) instantaneous kurtosis.

Figure 9 : (top) Seismic trace, (middle) AOK time-frequency representation, and (bottom) mean frequency of the seismic trace.

Figure 10 : (a) Hilbert transform instantaneous frequency and (b) Hybrid linear/quadratic time-frequency instantaneous frequency.

Figure 11 : (a) Time slice of 3-D data cube, (b) (x, t) cross-section through 3-D data volume, (c) (y, t) cross-section through 3-D data volume. (d)—(f) constant temporal frequency slices through the 3-D pseudo-Wigner distribution at locations denoted A, B, and C in slices (a)—(c), respectively. (g) (x, p_x) spectrum along a line of constant y through B. (h) (y, p_y) spectrum along a line of constant x through A.

Figure 12 : Volume attributes of the time slice of Fig. 11(a). (a) Local average slope in the x direction, (b) local average slope in the y direction, (c) modulus slope (volume dip), and (d) azimuth angle.

Figure 13 : (a) Seismic time slice and (b) local average slope in the x direction. Downward slopes are black.

Figure 14 : (a) Volume dip and (b) azimuth attributes of the time slice of Fig. 13(a).

Figure 15 : Comparison of attribute images, obtained using different local Radon spectra, of the time slice of Fig. 13(a). Volume dip images obtained using (a) spectrogram, (b) pseudo-Wigner distribution, (c) modified Wigner distribution, and (d) smoothed pseudo-Wigner distribution.

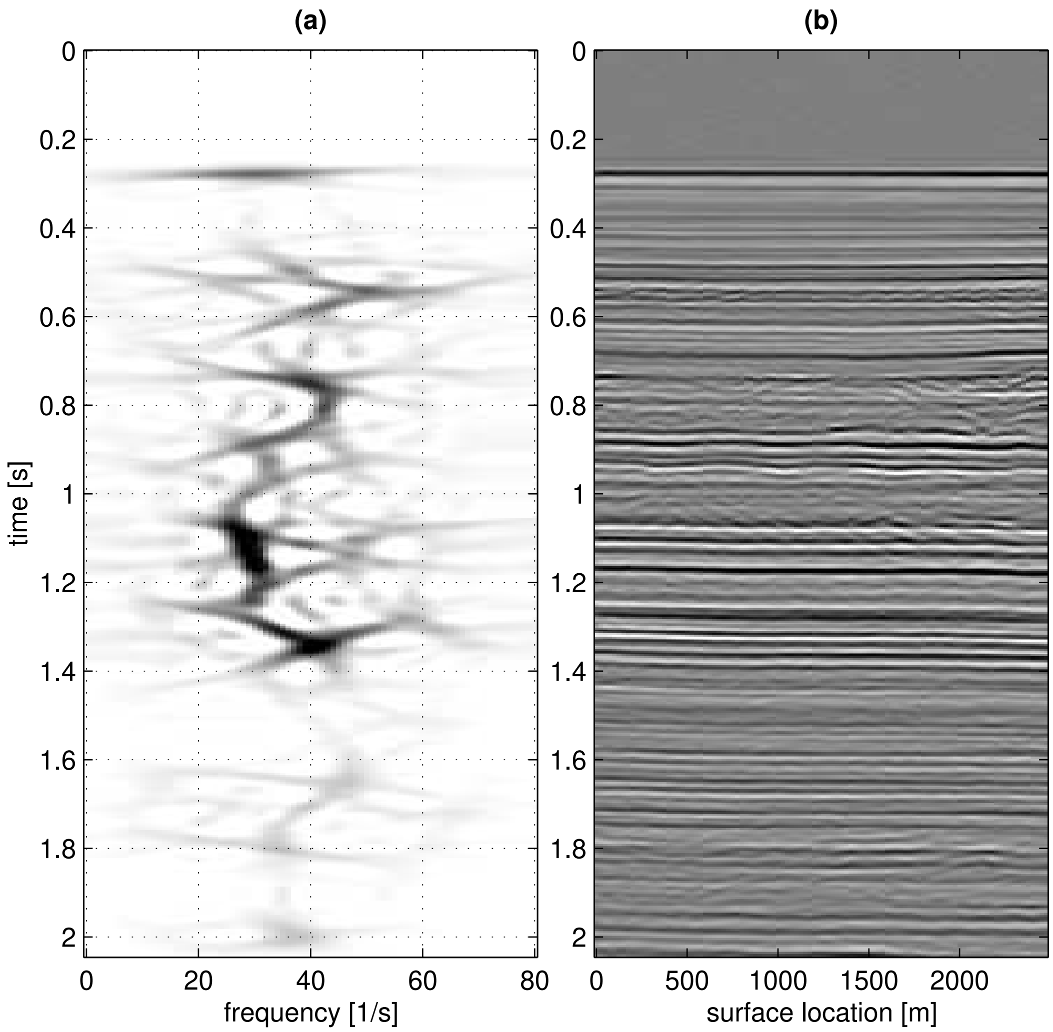
(a)
(b)
time [s]
frequency [1/s]
surface location [m]
0
0.2
0.4
0.6
0.8
1
1.2
1.4
1.6
1.8
2
20
40
60
80
500
1000
1500
2000

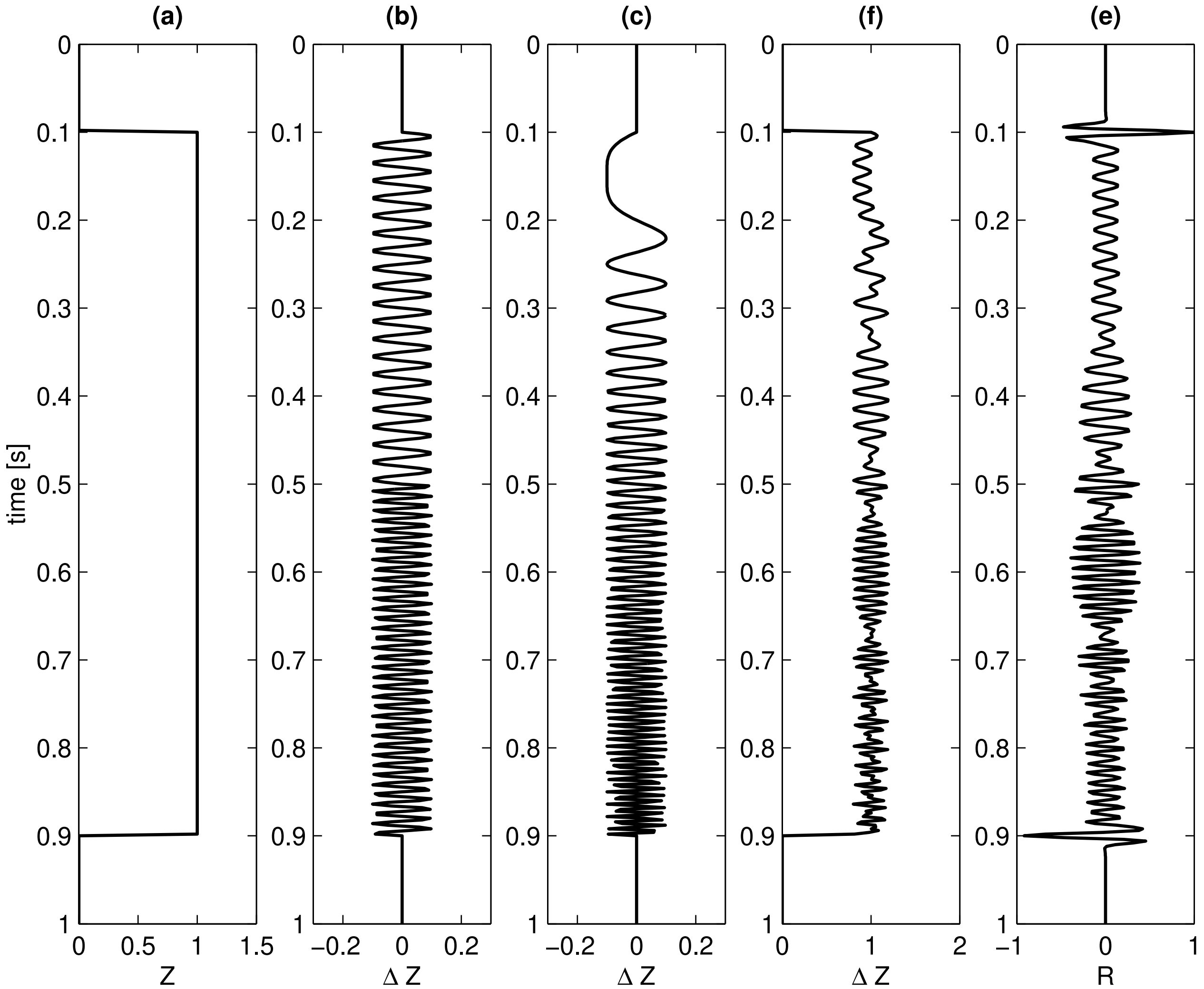

(a)
(b)
(c)
(f)
(e)
time [s]
0
0.1
0.2
0.3
0.4
0.5
0.6
0.7
0.8
0.9
1
0
0.5
1
1.5
Z
−0.2
0
0.2
Δ Z
−0.2
0
0.2
Δ Z
0
1
2
Δ Z
−1
0
1
R

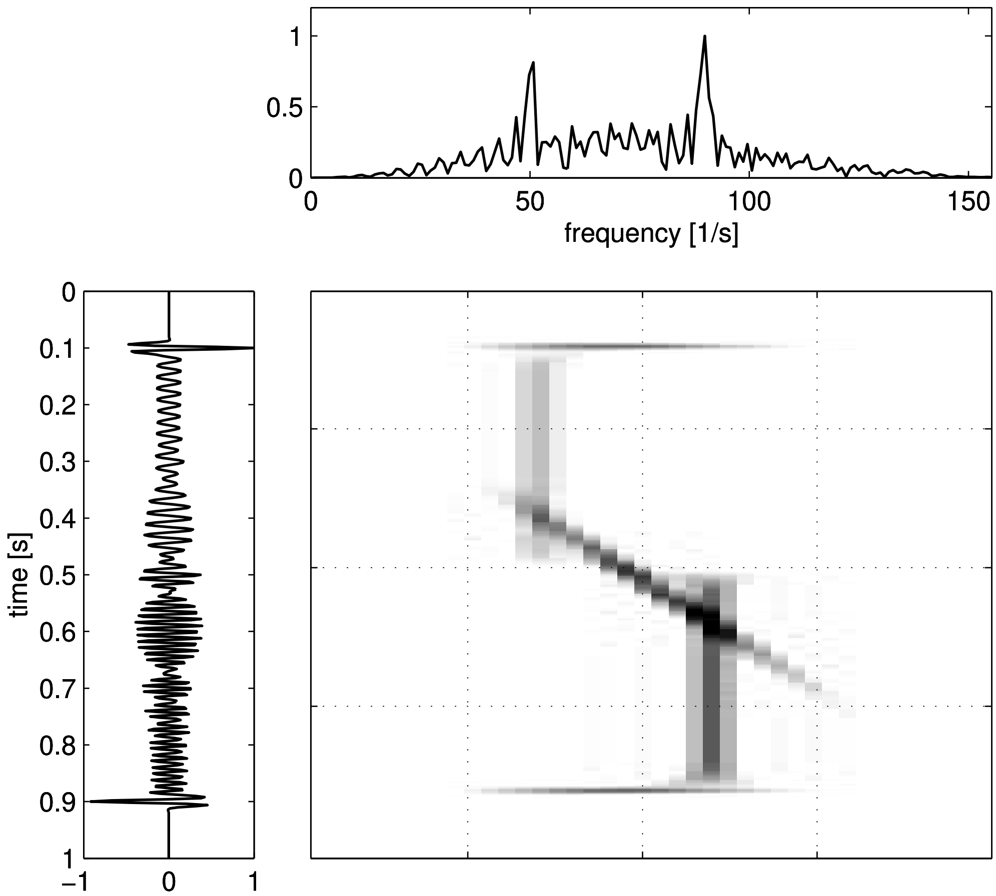
1
0.5
0
0
50
100
150
frequency [1/s]
0
0.1
0.2
0.3
0.4
0.5
0.6
0.7
0.8
0.9
1
time [s]
−1
0
1

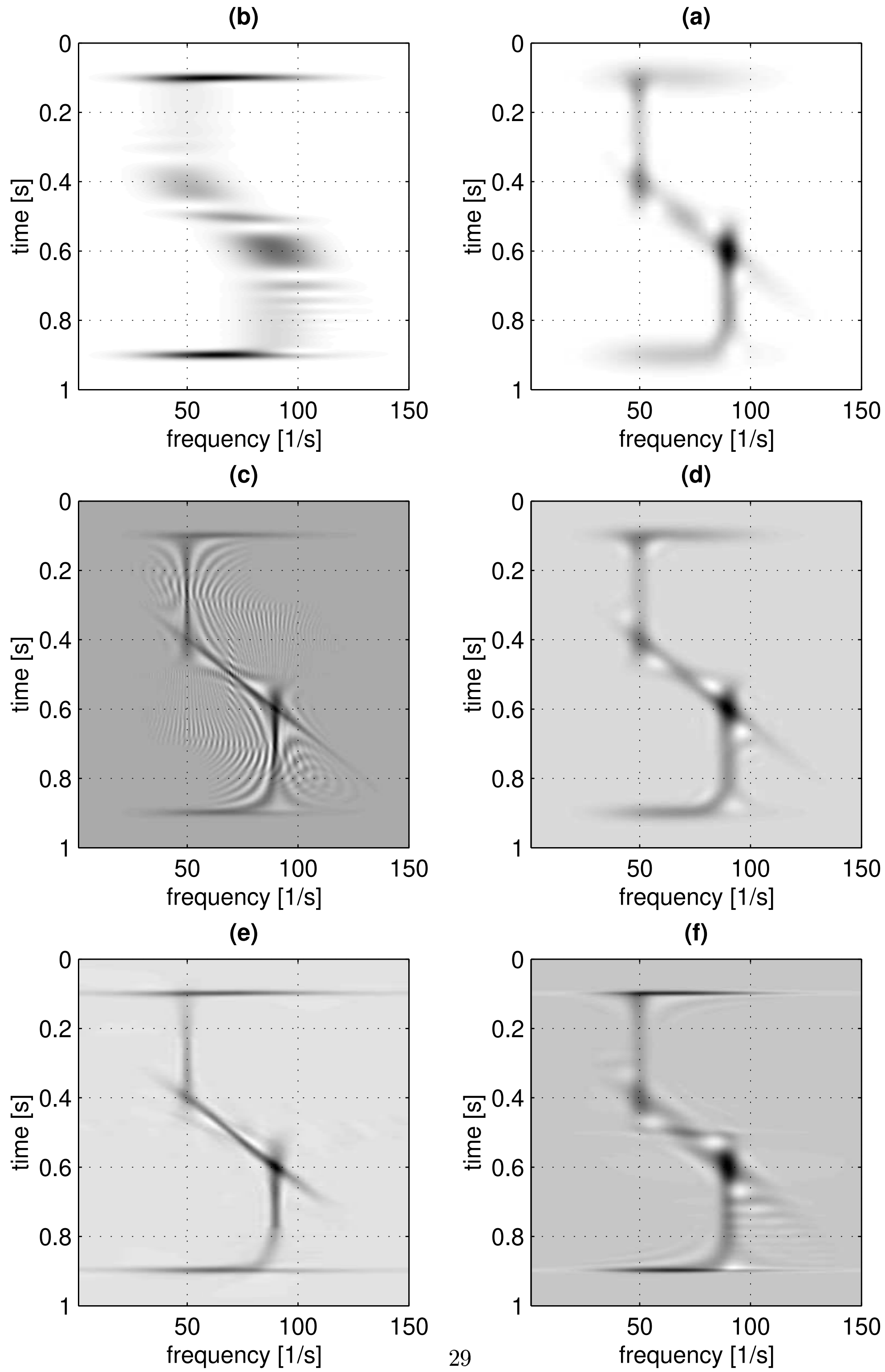
(b)
(a)
(c)
(d)
(e)
(f)
time [s]
frequency [1/s]
0
0.2
0.4
0.6
0.8
1
50
100
150

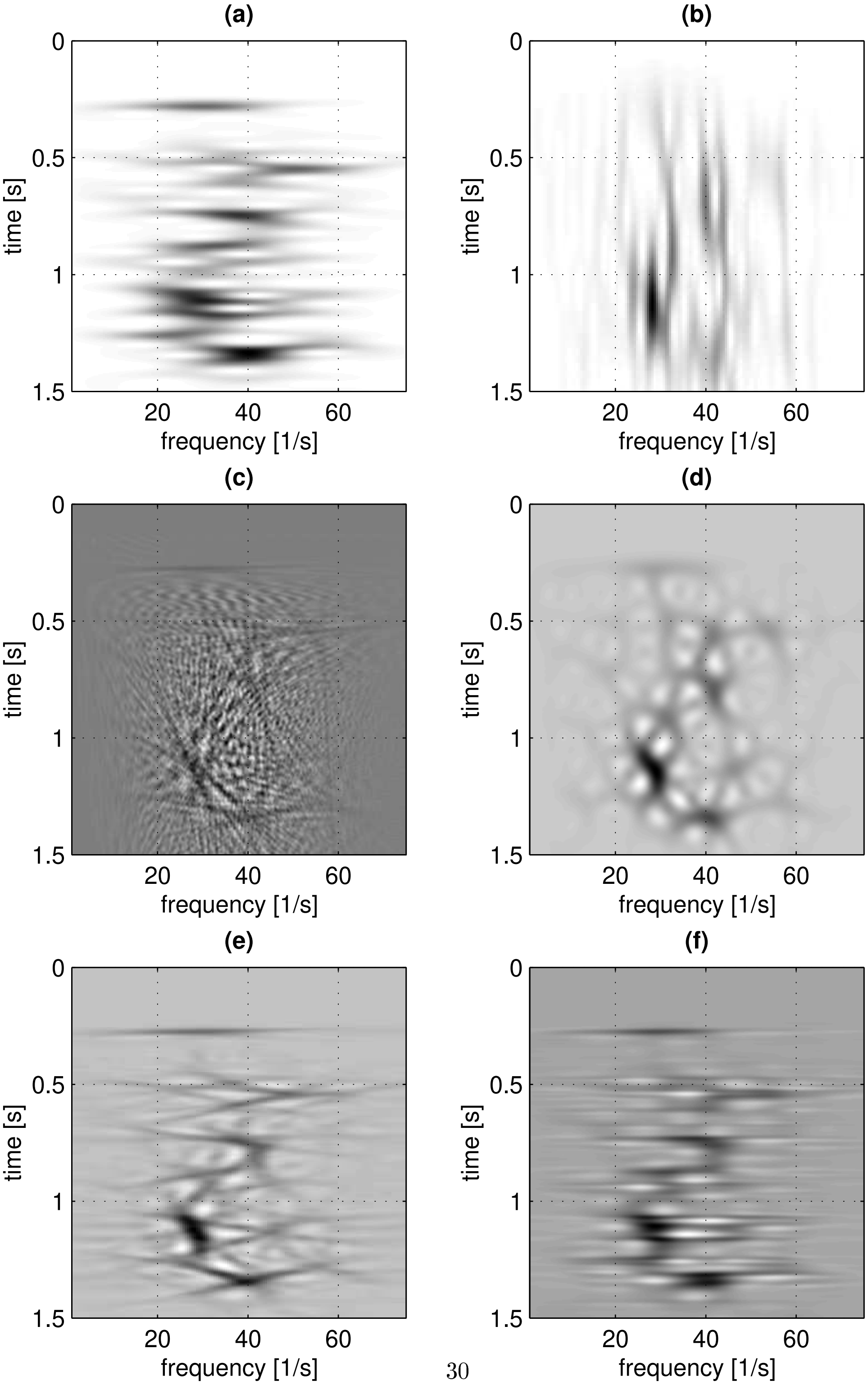
(a)
(b)
(c)
(d)
(e)
(f)
time [s]
frequency [1/s]
0
0.5
1
1.5
20
40
60

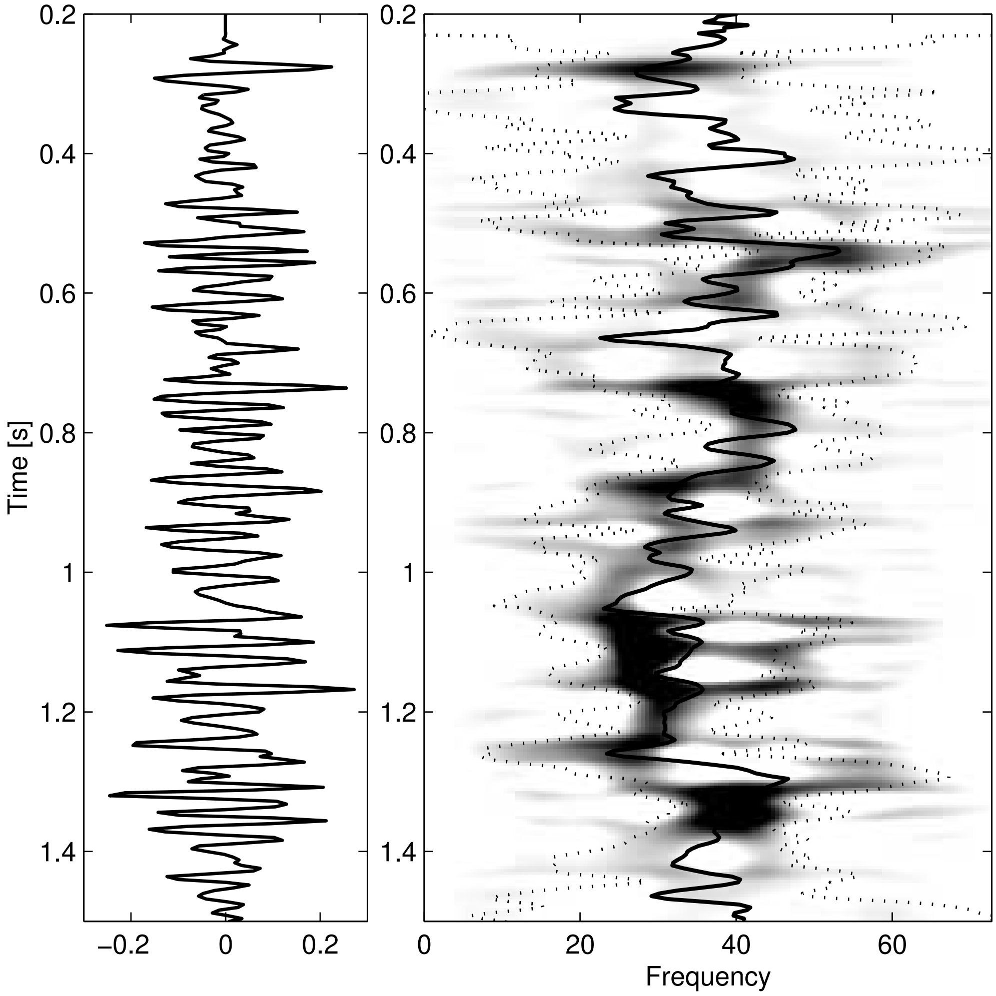
Time [s]
0.2
0.4
0.6
0.8
1
1.2
1.4
−0.2
0
0.2
0.2
0.4
0.6
0.8
1
1.2
1.4
0
20
40
60
Frequency

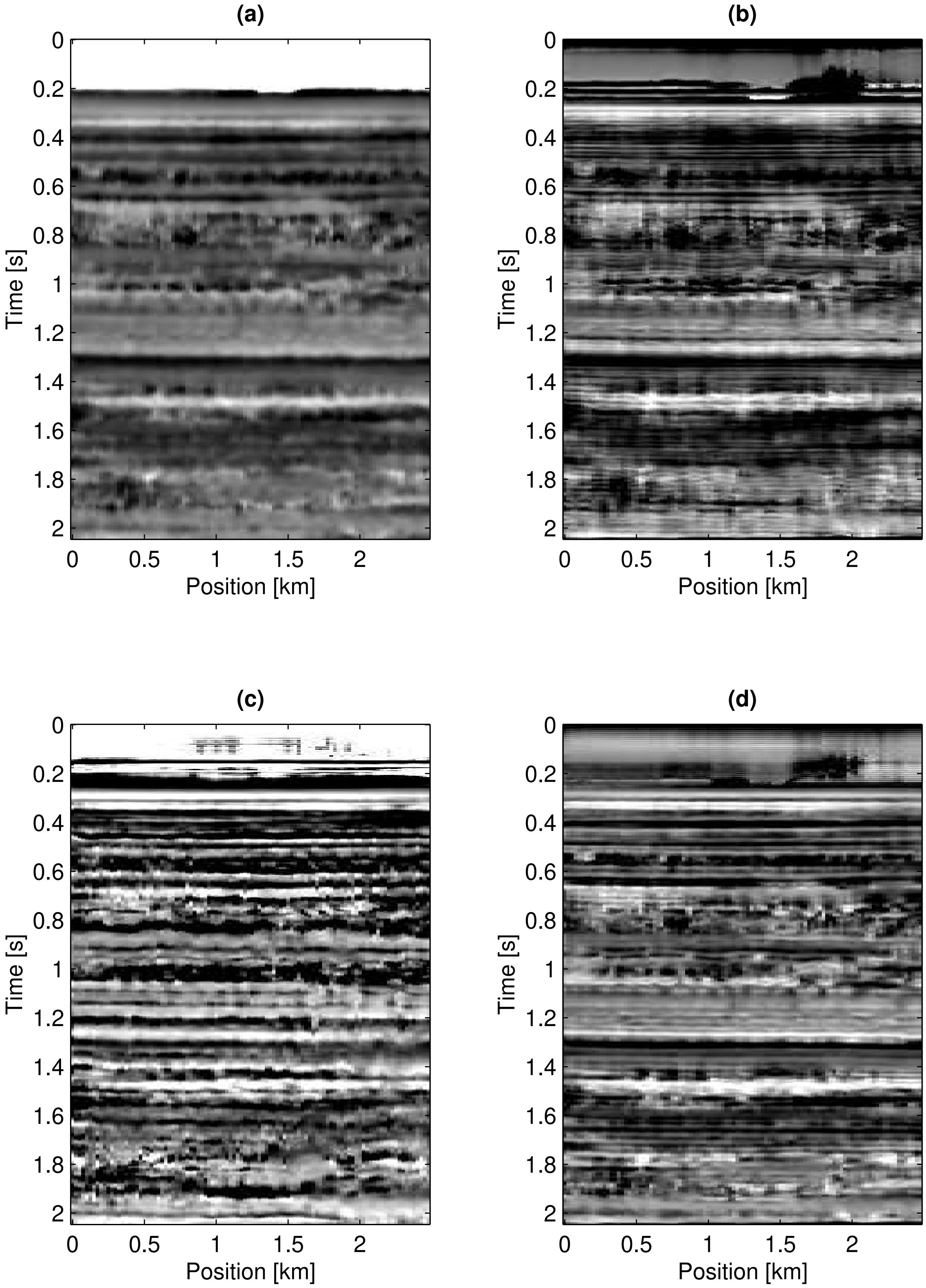
(a)
(b)
(c)
(d)
Time [s]
Position [km]
0
0.2
0.4
0.6
0.8
1
1.2
1.4
1.6
1.8
2
0.5
1.5

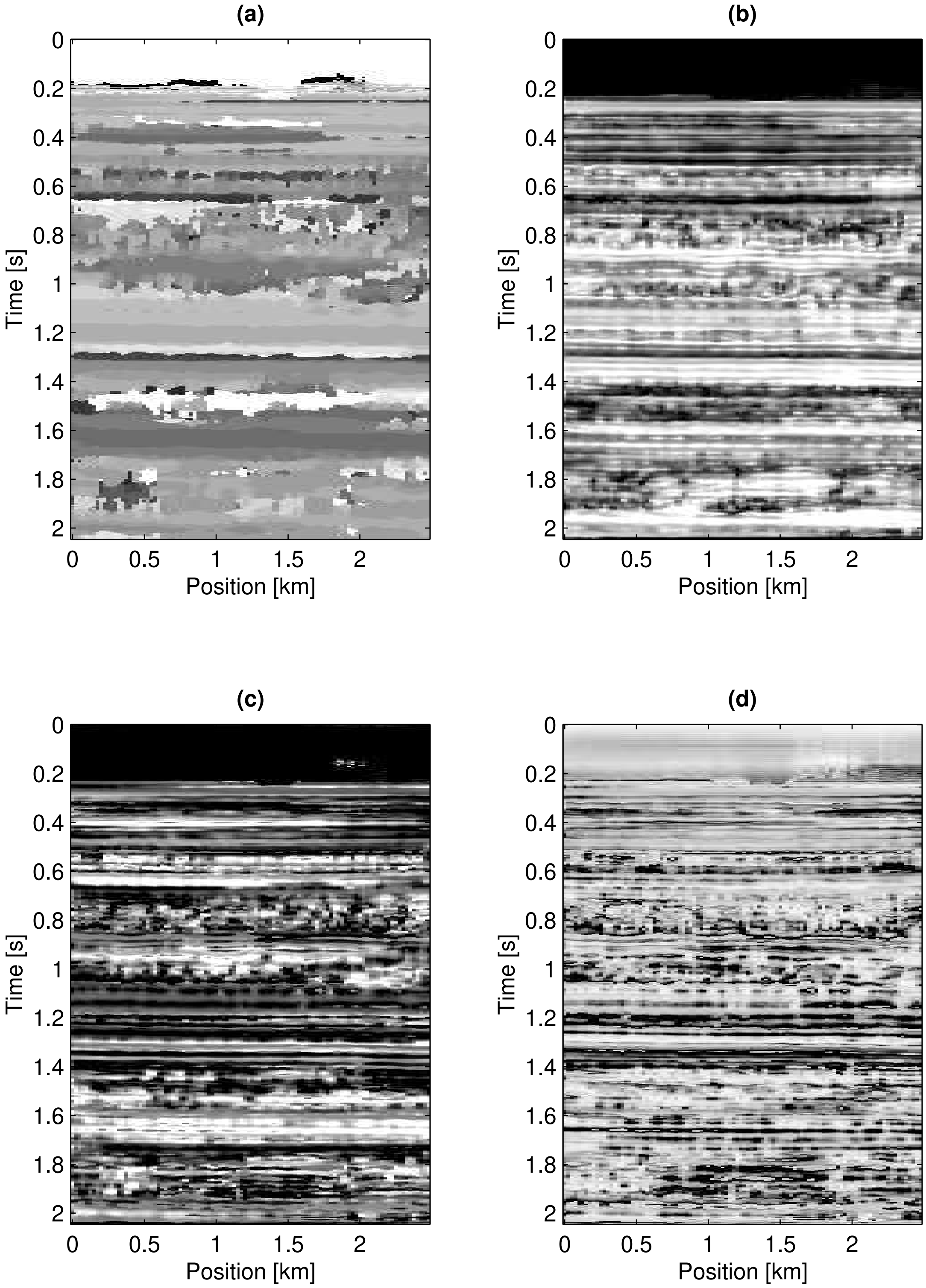
(a)
(b)
(c)
(d)
Time [s]
Position [km]
0
0.2
0.4
0.6
0.8
1
1.2
1.4
1.6
1.8
2
0.5
1.5

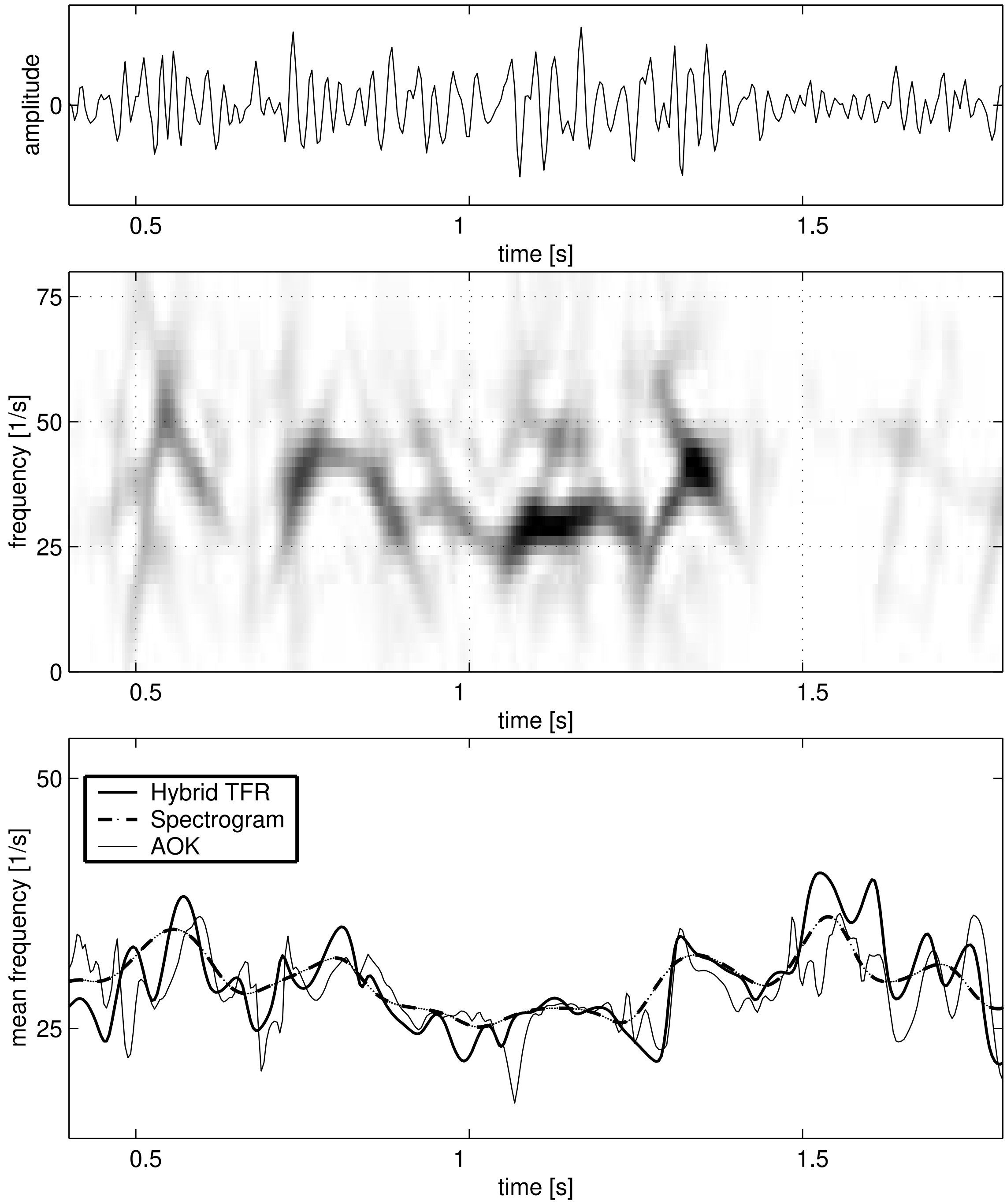

amplitude
0
0.5
1
1.5
time [s]
frequency [1/s]
75
50
25
0
0.5
1
1.5
time [s]
mean frequency [1/s]
50
25
Hybrid TFR
Spectrogram
AOK
0.5
1
1.5
time [s]

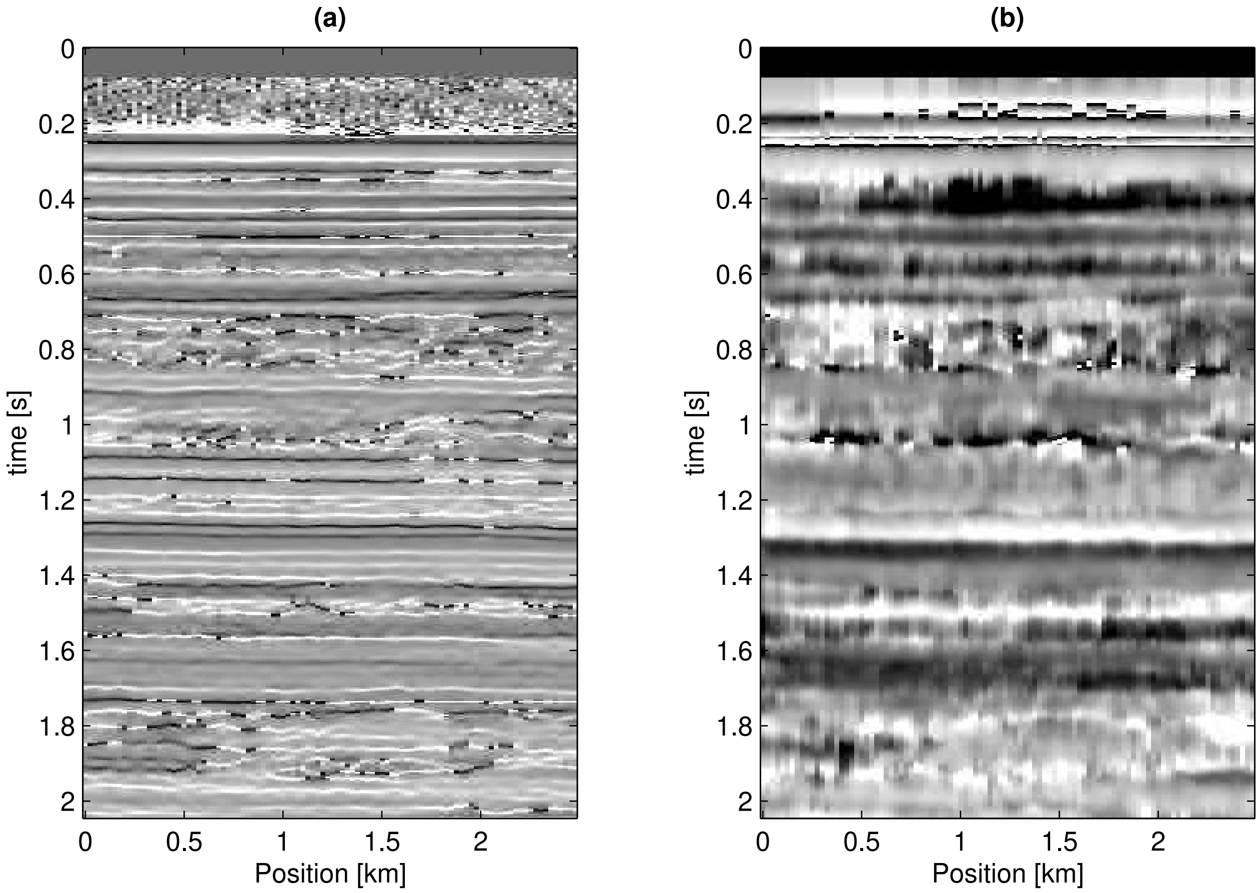
(a)
(b)
time [s]
Position [km]
0
0.2
0.4
0.6
0.8
1
1.2
1.4
1.6
1.8
2
0
0.5
1
1.5
2

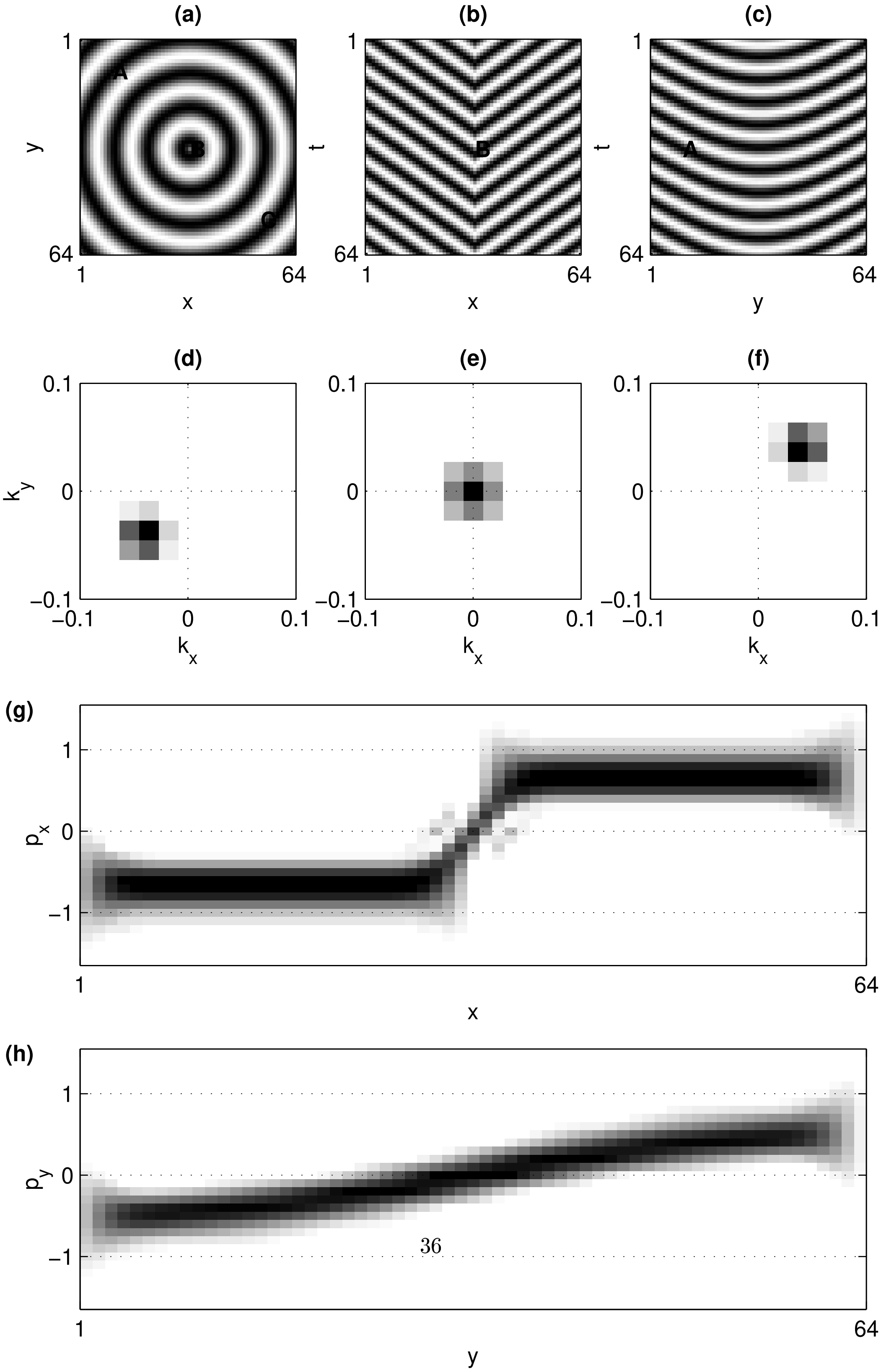

(a)
(b)
(c)
A
B
C
y
t
x
1
64
(d)
(e)
(f)
k_y
k_x
0.1
0
−0.1
(g)
p_x
(h)
p_y

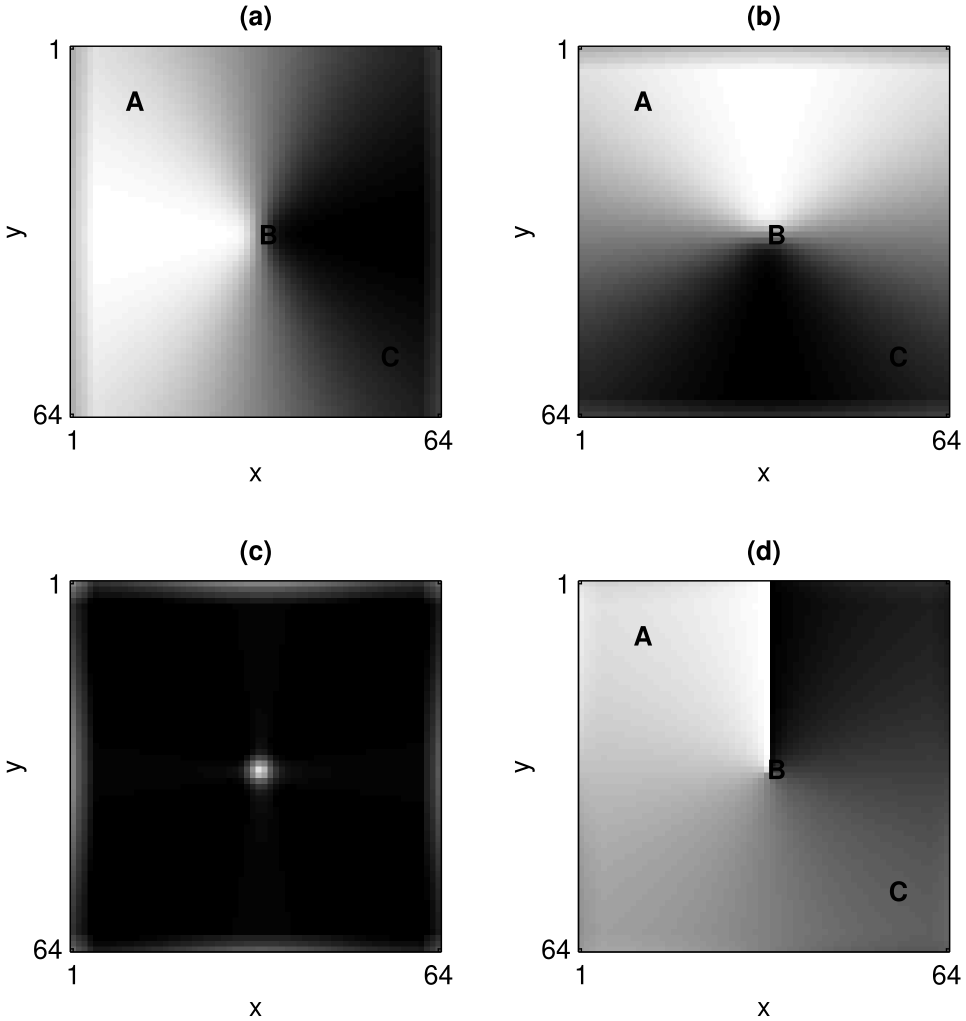
(a)
(b)
(c)
(d)
A
B
C
x
y
1
64

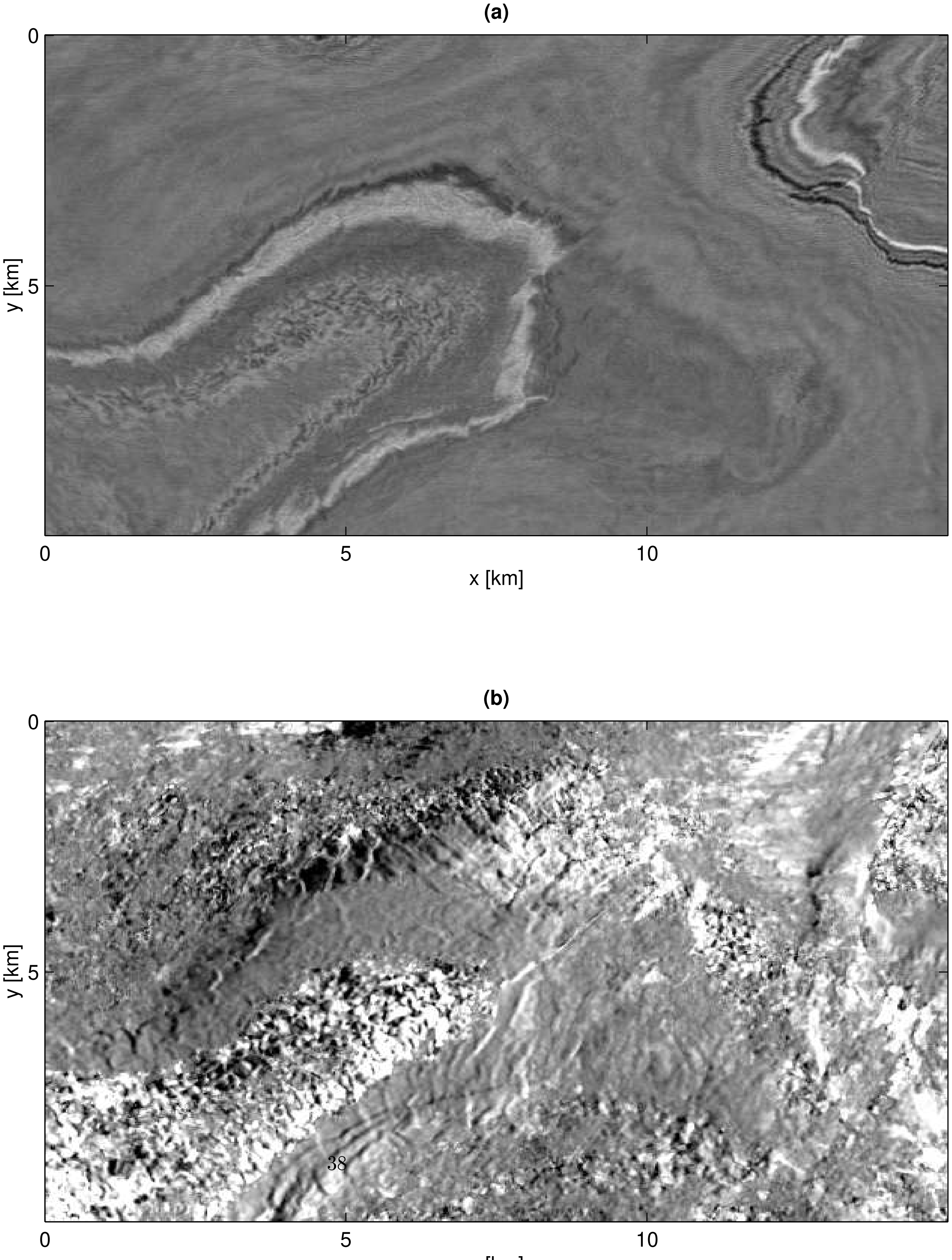
(a)
0
5
y [km]
0
5
10
x [km]
(b)
0
5
y [km]
0
5
10
x [km]

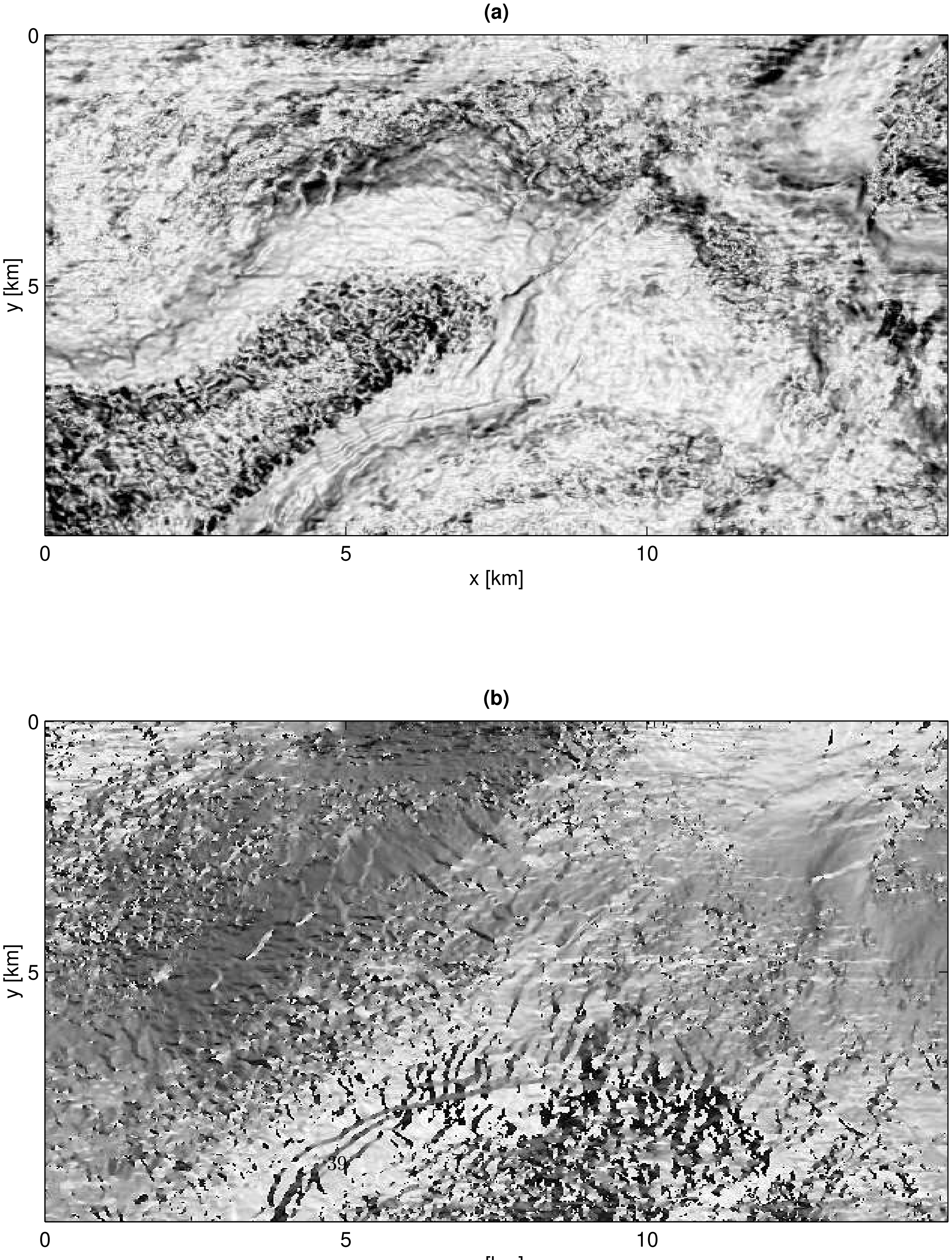
(a)
0
5
y [km]
0
5
10
x [km]
(b)
0
5
y [km]
0
5
10
x [km]

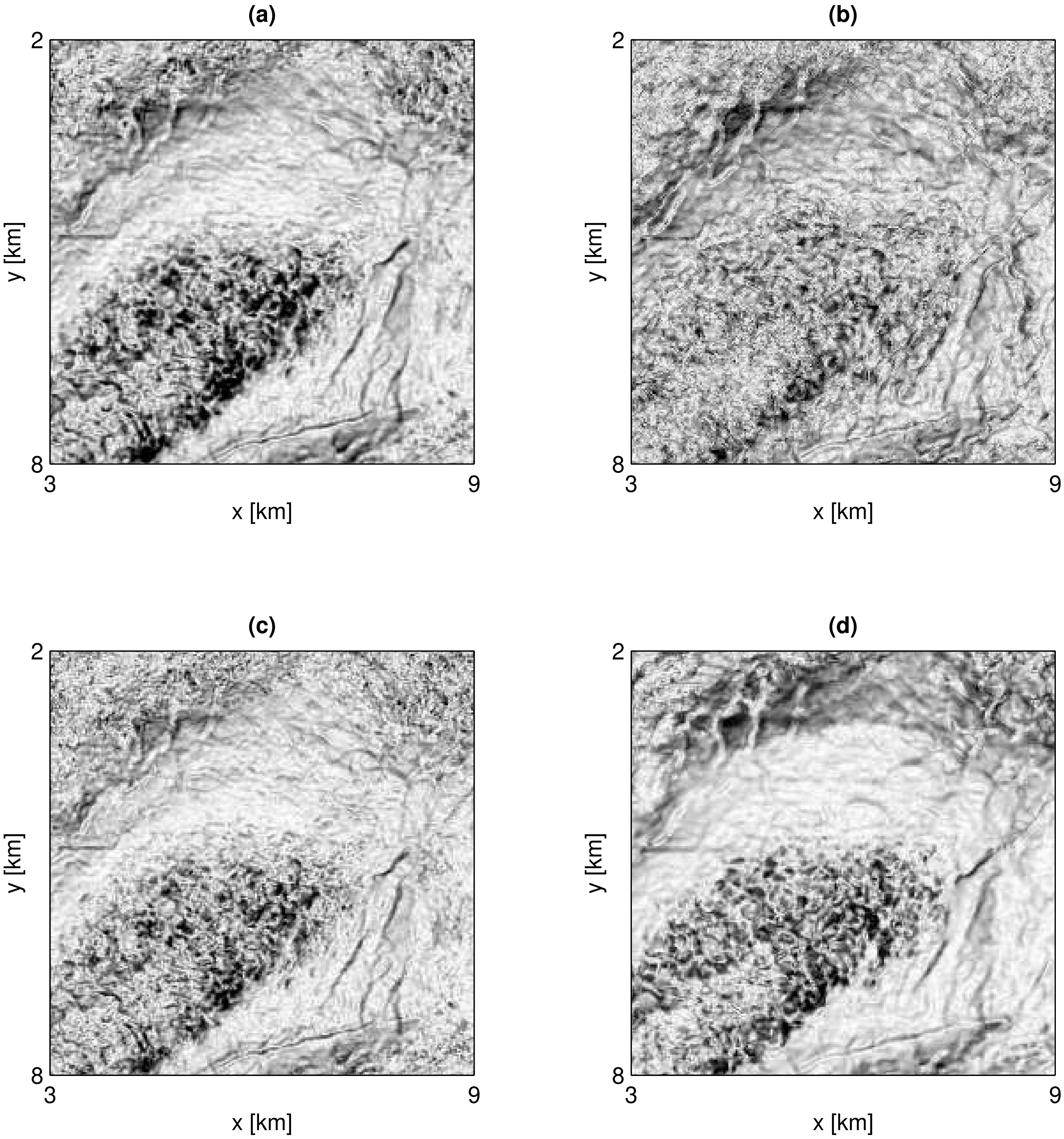
(a)
(b)
(c)
(d)
y [km]
x [km]
2
8
3
9